The latest advances in mass spec technologies. Designed for the masses.

Now available on-demand!

Scale up your research and translate your results more rapidly and simply than ever before with vLC-MS.com - the event for Thermo Scientific™ Orbitrap Exploris™ mass spectrometers and much more!

Tune in to:

- Explore the LC-MS portfolio and meet the expanded Thermo Scientific Orbitrap Exploris MS system in our Exhibit Hall.
- Learn from mass spectrometry experts, such as Professor Alexander Makarov himself, about Orbitrap mass spectrometry technology and the applications it enables.
- Browse posters and short presentations in your application area.

Event Highlights:

Prof. Alexander Makarov

Dr. Khatereh Motamedchaboki

Dr. Timothy Garrett

vLC-MS.com

WILEY

Md Fokhrul Islam[1]
Yiing C. Yap[1,2]
Feng Li[1]
Rosanne M. Guijt[3]
Michael C. Breadmore[1]

[1]Australian Centre for Research on Separation Science (ACROSS), School of Natural Science, University of Tasmania, Tasmania, Australia
[2]Menzies Institute for Medical Research, University of Tasmania, Tasmania, Australia
[3]Centre for Rural and Regional Futures, Deakin University, Geelong, Australia

Received February 19, 2020
Revised July 15, 2020
Accepted August 4, 2020

Research Article

The influence of electrolyte concentration on nanofractures fabricated in a 3D-printed microfluidic device by controlled dielectric breakdown

Abstract A three-dimensional-printed microfluidic device made of a thermoplastic material was used to study the creation of molecular filters by controlled dielectric breakdown. The device was made from acrylonitrile butadiene styrene by a fused deposition modeling three-dimensional printer and consisted of two V-shaped sample compartments separated by 750 µm of extruded plastic gap. Nanofractures were formed in the thin piece of acrylonitrile butadiene styrene by controlled dielectric breakdown by application voltage of 15–20 kV with the voltage terminated when reaching a defined current threshold. Variation of the size of the nanofractures was achieved by both variation of the current threshold and by variation of the ionic strength of the electrolyte used for breakdown. Electrophoretic transport of two proteins, R-phycoerythrin (RPE; <10 nm in size) and fluorescamine-labeled BSA (f-BSA; 2–4 nm), was used to monitor the size and transport properties of the nanofractures. Using 1 mM phosphate buffer, both RPE and f-BSA passed through the nanofractures when the current threshold was set to 25 µA. However, when the threshold was lowered to 10 µA or lower, RPE was restricted from moving through the nanofractures. When we increased the electrolyte concentration during breakdown from 1 to 10 mM phosphate buffer, BSA passed but RPE was blocked when the threshold was equal to, or lower than, 25 µA. This demonstrates that nanofracture size (pore area) is directly related to the breakdown current threshold but inversely related to the concentration of the electrolyte used for the breakdown process.

Keywords:
3D Printing / Controlled dielectric breakdown / Electrophoretic separation / Microfluidic device / Nanofractures
DOI 10.1002/elps.202000050

Additional supporting information may be found online in the Supporting Information section at the end of the article.

1 Introduction

Nanostructures can be fabricated within microfluidic devices and used in a diverse range of applications in chemical, electrical, and biological science [1–4]. Important applications for these nanostructures are in chemical sensors and biosensors. Nanostructures can increase device specificity with surface functionalization methods to improve detection sensitivity with high surface areas and to speed up sample delivery with nanofluidic techniques [5,6]. During the last 10 years, 1D nanostructures have been widely used in the field of biological science for the detection of various biomolecules [7–9]. Nanochannels offer great potential for optical detection in applications such as preconcentration [10], mixing [11], and DNA manipulation [12].

There are several techniques available to fabricate nanostructures, the most commonly used methods include electron beam lithography (EBL) and etching [13–15] and focused ion beam (FIB) drilling [16–18]. Nanoporous membranes have also been used in microfluidics for sample filtration, sample preconcentration, sensing, and selective

Correspondence: Professor Michael C. Breadmore, Australian Centre for Research on Separation Science (ACROSS), School of Natural Science, University of Tasmania, Private Bag 75, Hobart, Tasmania 7001, Australia
E-mail: Michael.Breadmore@utas.edu.au

Abbreviations: **ABS**, acrylonitrile butadiene styrene; **CAD**, computer-aided drawing; **f-BSA**, fluorescamine-labeled BSA; **FDM**, fused deposition modeling; **HPMC**, hydroxypropylmethyl cellulose; **RC**, resistor–capacitor; **ROI**, region-of-interest; **RPE**, R-phycoerythrin

Color online: See article online to view Figs. 1–4 in color.

delivery [19–21]. Conventional nanofabrication techniques rely on the production of nanopores in a vacuum environment, which inevitably introduces handling risks and wetting issues when transitioning into aqueous solutions for biosensing experiments [22]. Nanofractures can also be formed by dielectric breakdown, where thermal and mechanical failure results when an insulator is placed in an electric field exceeding its dielectric strength [23–28]. While this is a very simple and cost-effective technique for creating nanopores between two microfluidic chambers, the repeatability is highly variable because of the chaotic and almost random breakdown of the material. Previously, a few research groups have demonstrated the ability to control the size of the fractures produced in the breakdown of plastic by setting a current threshold, which terminates the voltage once a particular current is reached [23,26–30]. It is safe, tuneable, very fast, and allows creation of the nanofractures after fabrication of a complete fluidic device. This means it may be possible to create nanofractures after the sample is placed into a manufactured device that has been prefilled and packaged with all the reagents needed for the analysis.

Three-dimensional (3D) printing has gained significant attention in manufacturing due to its ability to manufacture 3D designs by retrieving computer-aided drawing (CAD) files without the need of conventional microfabrication. The past few years has seen significant improvements in the techniques of 3D printing technology that is now been adapted to work with a diverse range of materials including production-grade plastics, metals, and glass. As a result, this technology is not only being used in constructing a mold for prototyping but also being used in manufacturing approach [31]. Recently, several 3D printing techniques have been used to fabricate microfluidics chips, with the most common being stereolithography [32–35], fused deposition modeling (FDM) [36,37], and photopolymer inkjet printing [38,39]. Here, we used FDM 3D printing to fabricate fluidic devices because they can be printed in production-compatible thermoplastic material that can be used for large-volume manufacturing. A wide range of thermoplastic materials are available for FDM 3D printers, including acrylonitrile butadiene styrene (ABS), polylactic acid, polycarbonate, polyamide, and polystyrene, which provide a wide range of physicochemical and mechanical properties and hence a choice of color, optical transparency, and chemical and biological compatibility. Multimaterial FDM printers can also be used to produce devices containing components or regions of greatly differing strength, flexibility, porosity, electrical conductivity, etc. One area of considerable interest is the ability to print materials of controlled or selective porosity, including active and passive integrated membranes [20,40–44]. Despite the success in creating quite complex devices, the pore properties are defined by the material used and there is no easy way to vary their properties.

In this paper, we used controlled dielectric breakdown to fabricate nanofractures in an FDM-printed fluidic device. The device was made using the thermoplastic material ABS and the nanofractures created by termination of the breakdown voltage once a threshold current was reached. Different current limits in different electrolyte concentrations were examined to understand the impact of a variation in the sample matric composition if nanofractures were to be created after sample was placed into the device. The transport properties of the produced nanofractures were examined with two proteins, natively fluorescent R-phycoerythrin (RPE) and fluorescamine-labeled BSA (f-BSA).

2 Materials and methods

2.1 Materials and chemicals

Crystal clear ABS 1.75 mm filament (MatterHackers Inc; Foothill Ranch, CA) was used to print the device. RPE ($\geq$10 mg/mL, mW 250), BSA, fluorescamine, sodium phosphate dibasic, sodium phosphate monobasic, ferric chloride ($FeCl_3$), and hydroxypropylmethyl cellulose (HPMC, MW 26 kDa, Catalogue number 29441-1) were purchased from Sigma-Aldrich (St. Louis, MO). Potassium thiocyanate (KSCN) was purchased from AJAX Chemicals (Sydney, Australia). All the experimental solutions used in this study were prepared in milli-Q water obtained from a Millipore (North Ryde, Australia) purification system.

2.2 Sample Preparation

BSA stock solution was prepared with a concentration of 2 mg/mL in milli-Q water. Fluorescamine solution was prepared with a concentration of 3 mg/mL in acetone as a stock solution. Immediately before the all experiment, f-BSA was freshly prepared by incubating the BSA stock solution and fluorescamine solution at the ratio of 3:1 in phosphate buffer for 15 min at room temperature. The 2.5 M of KSCN and 25 mM $FeCl_3$ solutions, and 1 mg/mL of RPE solution were prepared in milli-Q water.

2.3 Device design and fabrication

The microfluidic chip design was first drawn in AutoCAD 2016 (Student version; Autodesk, San Rafael, CA) and then exported as a STL file. The STL file was then sliced into multiple 2D layers using Kisslicer PRO (www.kisslicer.com) and then exported for printing as a g-code file. In this study, an FDM-based 3D printer (Felix 3.0; Felix robotics, The Netherlands) was used to print the microfluidic chip. The FDM printer extruded thermal plastic through a heated nozzle, which was controlled by two precision stepper motors, following coordinates specified by g-code generated using Kisslicer, using the following parameters: layer height 100 µm, extrusion width 0.2 mm, infill 100%, print speed 30 mm/s. A previous study demonstrated that devices that printed with the filament extruded parallel (0°) to the flow had better laminar fluidic behavior [45]. Therefore, the nozzle movement in the slicing software was also adjusted such

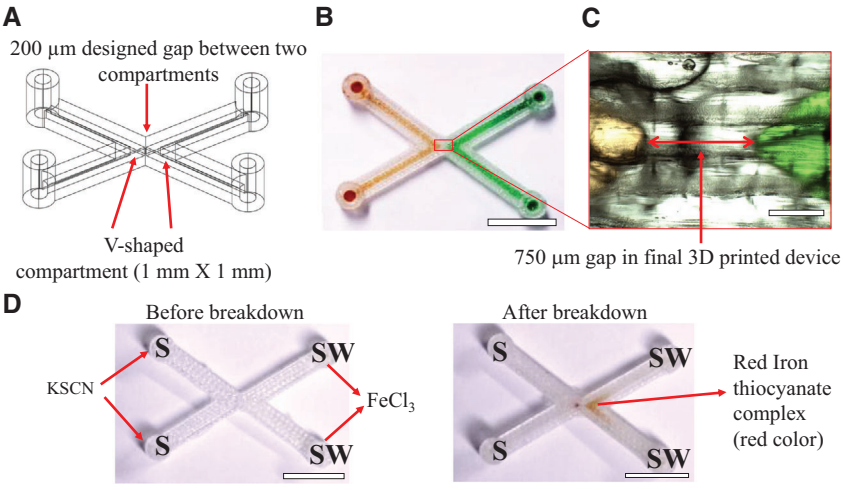

Figure 1. (A) CAD illustration showing the dimensions of the two V-channels and the gap distance between the two V-channels. (B) Photograph image of the two V-shaped 3D-printed ABS device filled with yellow food dye on the left V-channel and green food dye on the right V-channel. Scale bar = 10 mm. (C) Zoomed in microscope image of the double V-channel. Red box in panel (B). Scale bar = 325 µm. (D) Two sample reservoirs (S) and two sample waste reservoirs (SW) were filled with $FeCl_3$ and KSCN solution, respectively. Before breakdown, no changed was observed. After breakdown, these two chemicals came into contact and the red iron thiocyanate complex (red color) formed. The red color formation in the gap between the two compartments indicates the presence of nanofractures. Scale bar = 10 mm.

that the filament was extruded at angles of 0° (parallel) to the fluid flow of the channel and printing the left V-shaped channel followed by the right V-shaped channel. After printing each layer, the build platform was lowered 100 µm before extruding the next layer. A single nozzle was used to extrude clear ABS at a temperature of 220°C while the print bed was at 70°C throughout the print. No support material was used. A schematic of the device design is shown in Fig. 1A, with the V-channel dimension of 1 × 1 mm with 200 µm gap between the tips of the V-channels. For the measurement of fabrication channels, Image J software (NIH, USA) was used.

2.4 Dielectric breakdown process

Breakdown electrolyte solution (1 mM, 10 mM, 100 mM, 250 mM, 500 mM or 1000 mM phosphate buffer, pH 7) was filled into both of the two V-shaped microchannels. Before breakdown, a handheld digital multimeter (RS Components Pvt. Ltd., NSW, Australia) was used to measure the fluidic resistance of two microchannels and confirmed there was no connection between the two V-shaped channels. Electrodes were placed in the reservoirs and voltage was applied using an in-house built high-voltage power supply controlled via a Labview program (National Instruments, Austin, TX, USA). Data acquisition and automation measurement were performed using this program via a National Instrument USB 6212 board. Using this program, the voltage output was set at 1 kV increment at every 10 s while monitoring the return current and keeping the current at the threshold defined by the user. In addition, the Labview was also set to automatically reduce the voltage to zero when it detected the current increasing. Once the desired current level was obtained, the applied voltage was terminated as controlled by the Labview software, which prevented further breakdown of the material and enlargement of the existing formed nanofractures and/or creation of more nanopores. In this study, the breakdown process was terminated at threshold currents of 50 µA, 25 µA, 10 µA, 5 µA, or 1 µA at the final applied voltage. A sharp increase in current was observed, which indicated the occurrence of distinct breakdown event, as shown in current and voltage versus time graph at breakdown condition of 25 µA threshold current in 1 mM phosphate buffer, pH 7 (Supporting Information Fig. S1A). The bias voltage of ~0 kV using our in-house make power supply system was observed in the current–voltage curve at different breakdown condition at approximately 600 ms before the desired current though the applied voltage only terminated when the set threshold current obtained as controlled by the Labview software. In addition, there was ≥0.8 µA of current was leaked through the plastic before the breakdown as seen in the zoomed current versus time graph (Supporting Information Fig. S1B). After breakdown, all devices were filled with $FeCl_3$ and KSCN solution, respectively, in two separate chambers to investigate the presence of nanofractures.

2.5 Electrokinetic transport

To evaluate the electrokinetic transport properties of two different sizes of proteins (RPE and f-BSA) through the nanofractures, 10 mM phosphate buffer at pH 11.5 and 0.5% HPMC were used as background electrolyte solution. The 0.5% HPMC was added in order to suppress the EOF [27]. The natively fluorescent RPE (isoeletric point of 4.1–4.2) and f-BSA have a net negative charge at pH higher than their isoelectric point and migrated toward the anode (positive charge), hence pH 11.5 was chosen during electrophoresis process. After nanofracture creation, the V-shaped sample compartments (S) were filled with 10 mM phosphate buffer, 0.5% HPMC at pH 11.5, and samples solution. The voltage was applied for 180 s using external electrodes for each reservoir, with the sample reservoirs (S) of the left V-channel applied at −200 V and the opposite sample waste reservoirs (SW) of the right V-channel applied at +200 V. Visualization of the movement of the fluorescent molecules was observed using an inverted fluorescence microscope (Nikon Eclipse Ti,

Nikon, Tokyo, Japan) integrated with Nikon high-definition color CCD camera head (Digital Sight DS-Filc, Nikon, Japan) and operated with NIS-Elements BR 3.10 software (Melville, NY, USA). An in-house four-channel (0−5 kV) DC power supply was used to apply the indicated electrical potentials to each reservoir. Multiband pass excitation (λ_{ex} at 390, 482, 563, and 640 nm) and emission (λ_{em} at 446, 523, 600, and 677 nm) filters (Semrock, Rochester, NY, USA) were used to capture all fluorescent images and videos. Mean fluorescence intensities within a specified region-of-interest (ROI) of the sample at opposite sample waste reservoirs (SW) of the right V-channel over time were analyzed with image J software (NIH, USA). In addition, we defined "passing" of protein molecules through nanofractures when the value of $(F - F_o)$ is greater than zero and "restricted" when the value of $(F - F_o)$ equals zero, where F is defined as the mean fluorescence intensity within a specified ROI of the sample in the SW reservoir in the right V-channel at time $t = 180$ s and F_o is the baseline fluorescence intensity in the same position at time zero. In this study, three devices from different breakdown conditions were used for each analysis. The same device was used to evaluate both RPE and f-BSA protein transport properties through the nanofractures, rinsing the device with Milli-Q water at least three times after each test.

3 Results and discussion

Our previous work on controlled dielectric breakdown demonstrated control of the size of the nanofractures produced by terminating the voltage once a defined current threshold had been reached [23]. This was used to create size and mobility nanofractures to purify and concentrate therapeutic drugs from whole blood prior to electrophoretic separation and analysis of the target drugs within the same device [23,26,27]. We envisage creating the nanofractures after fabrication of the device once it is filled with sample, however, variation in the sample matrix could change the nanofractures produced. Our aim was to understand how much these would be influenced by ionic strength changes and whether usable devices could be obtained with a fixed current breakdown or whether we would need to measure the conductivity of the sample first to select the appropriate breakdown threshold to obtain a fracture of a desired transport range.

The devices used were created from ABS using an FDM printer. ABS is a very common low-cost thermoplastic material. It is strong and durable and has moderate optical transparency in the visible region of the spectrum with little or no autofluorescence, allowing simple visual inspection of the breakdown performance [46]. Our FDM printer is suitable for microfabrication with minimum features of 321 ± 5 µm [31]. Thus, the smallest physical gap to separate two fluidic chambers was approximately 750 µm, using a CAD design of 200 µm. It was not possible to change this to be smaller while still ensuring fluidic separation between the two fluid chambers due to the way in which the software sliced the structure to construct the resulting FDM head movement, which began by printing an outline of the two V fluidic structures. A photograph of the 3D-printed device filled with food dye solutions (yellow and green) is shown in Fig. 1B and a zoomed microscope image of the double V-channel in Fig. 1C. Given the thickness of plastic separating the two fluidic V channels was 750 µm, a higher breakdown voltage was needed than previously reported. Shallan et al. applied 2.2 kV to breakdown PDMS (dielectric strength = 21 V/µm) [23] with a gap distance of 100 µm. This study required a higher voltage to be used (15–20 kV) to fracture the printed plastic device in a reasonable timeframe (<3 min) given the longer gap distance (750 µm) and the dielectric strength of 20–25 V/µm in ABS [47].

As the nanofractures are created by terminating the breakdown voltage once a specified current threshold is reached, variation in the conductivity of the solution should result in a different sized nanofracture based on the assumption that the voltage drop over the plastic is constant and therefore the current is related to the resistivity of the media filling the nanojunction that connects the two fluidic channels.

Our experimental setup can be considered as a physical resistor–capacitor (RC) circuit system, as shown in Supporting Information Fig. S2. When the voltage is applied to the system, the ABS wall (specifically the region between the two channels) will act as a capacitor while the electrolyte in the channels will act as resistors. Charge will start to accumulate on the ABS surface until its capacitance is reached, leading to charging current phenomena (also known as capacitor charging). When the capacitor is charging, the flow of charge is restrained or restricted by the electrical resistance of media (electrolyte concentration), which increases the time constant of the RC circuit system. As given by Eq. (1), the conductivity of the electrolyte affects the time required to charge the capacitors plates (defined as the time constant in the RC circuit). As the capacitor takes a longer time to charge, this impacts on the flow of current at the moment of breakdown. The threshold current—the after-breakdown current that is read by Labview software—is purely resistive circuit given by Eq. (2) as capacitor is shorted in RC circuit after breakdown, with R being the sum of the channel resistance and the electrical resistance of the current path through the created pores.

$$\mathrm{I_C} = \frac{V}{R} e^{\frac{-t}{RC}}, \tag{1}$$

$$I_B = \frac{V}{R}, \tag{2}$$

where V is applied voltage across the ABS chip, I_C is the charging current during breakdown, t is the elapsed time since application of the supply voltage, RC is the time constant of the RC charging circuit, R is the total resistance of the media (electrolyte solution), and I_B is the current after breakdown.

Different current limit (50, 25, 10, 5, or 1 µA) and different concentrations of electrolyte (1, 10, 100, 250, 500, or 1000 mM, pH 7) combinations were experimentally

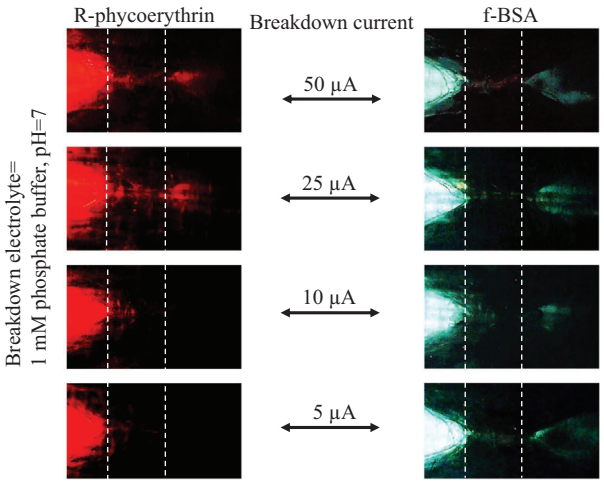

Figure 2. Screenshots shows the electrophoretic transport of protein R-phycoerythrin (RPE) (1 mg/mL) and fluorescamine-labeled BSA (f-BSA) (2 mg/mL) through the nanofractures created at a different breakdown current limit using 1 mM phosphate buffer, pH 7. Dashed lines were drawn at the tip of the V-channel to distinguish the region between the nanofractures and main compartments. The top two rows show the nanofractures formed at 50 μA and 25 μA permitted the transport of both RPE (left) and f-BSA (right) into the sample waste compartment. Third rows and fourth rows show the nanofractures formed at 10 μA and 5 μA, respectively, only permitted the transport of f-BSA but restricted the RPE. Scale bar = 750 μm. Each image is the representative of three devices from different breakdown conditions. Images of the same device are presented for both RPE and f-BSA.

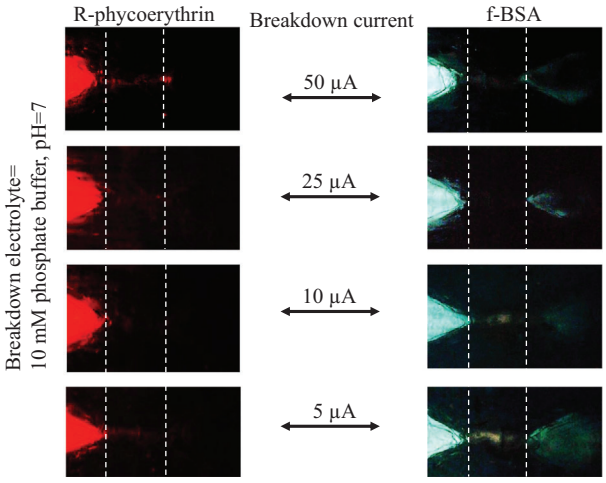

Figure 3. Screenshots shows the electrophoretic transport of protein R-phycoerythrin (RPE) (1mg/mL) and fluorescamine-labeled BSA (f-BSA) (2 mg/mL) through the nanofractures created at a different breakdown current limit using 10 mM phosphate buffer, pH 7. Dashed lines were drawn at the tip of the V-channel to distinguish the region between the nanofractures and main compartment. The top rows show the nanofractures formed at 50 μA permitted the transport of both RPE (left) and f-BSA (right) into the right, sample waste compartment. Second, third and fourth rows show the nanofractures formed at 25 μA, 10 μA and 5 μA, respectively, only permitted the transport of f-BSA but restricted the transport of RPE into the main sample waste compartment. Scale bar = 750 μm. Each image is the representative of three devices from different breakdown conditions. Images of the same device are presented for both RPE and f-BSA.

examined. In order to confirm or visualize the successful generation of nanofractures, the device was filled with $FeCl_3$ and KSCN solution at either side of the V-channels. Devices in which breakdown occurred resulted in observation of a red color from the iron thiocyanate complex formed in the gap within the two V-channel, indicating the transport of small inorganic ion (~ 0.3 nm), as illustrated in the representative photograph (Fig. 1D).

The permeability results of two different size proteins, natively fluorescent RPE (250 kDa; hydrodynamic radius of ~10 nm) [27] and f-BSA (66 kDa; hydrodynamic radius of ~4 nm) [27], were used to estimate the size of the fabricated nanofractures given the difficulty in finding the structures by SEM and other imaging techniques given that we have previously seen the nanofractures formed as a bundle of interconnected, highly variable, nonuniform size structures with rough surface. Fluorescamine was used to label the BSA because it reacts with primary amines in milliseconds to produce a fluorescent product while the excess unreacted reagent is hydrolyzed to a nonfluorescent neutral product effectively removing it from the reaction [48]. In order to minimize the risk of degradation of the fluorescent product after the labeling reaction, we prepared the f-BSA freshly before all the experiments.

Figure 2 shows the transport of RPE (left) and f-BSA (right) in devices made at different breakdown current thresholds using a 1 mM phosphate buffer, while Fig. 3 shows the same images with 10 mM phosphate buffer. In Fig. 2, the nanofractures formed at 50 μA and 25 μA permit the transport of both RPE and f-BSA, while those created at 10 μA and 5 μA restricted the transport of RPE but allowed f-BSA to pass. When using the 10 mM electrolyte, only when a 50 μA breakdown current was used did both proteins pass through the nanofractures, while all other conditions blocked the movement of RPE but allowing transport of BSA. Similar experiments were performed with phosphate buffer concentrations of 100, 250, 500, and 1000 mM, with an overview of the transport of RPE and f-BSA shown in Table 1. At all currents and electrolyte concentrations of 100 mM phosphate buffer and above, RPE was restricted from moving through the nanofractures while BSA was able to move through freely. It is noticeable in Fig. 3, second row, that nanofractures formed at 25 μA permitted the transport of protein RPE part way through the nanofractures but did not make it all the way through into the main channel. We believe that this is because the size and shape of the nanofractures are not uniform, as shown previously by Shallan et al. [23]. Due to the varied geometry of the nanofracture, migration of the RPE protein occurred into what we imaged to be a narrowing channel where they become stagnant where their smallest pore size prohibits further migration. Based on the permeability results of two different sized molecules (RPE ~10 nm, BSA 2–4 nm), we believe that, even though the fracture contains

Table 1. Electrophoretic transport of R-phycoerythrin (RPE) (1 mg/1 mL) and fluorescamine-labeled BSA (f-BSA) (2 mg/mL) through the nanofractures formed at different breakdown conditions

Breakdown current(μA)	Phosphate buffer concentration											
	1 mM		10 mM		100 mM		250 mM		500 mM		1000 mM	
	RPE	f-BSA	RPE	f-BSA	RPE	f-BSA	RPE	f-BSA	RPE	f-BSA	RPE	f-BSA
50	Passing	Passing	Passing	Passing	Restricted	Passing	Restricted	Passing	Restricted	Passing	Restricted	Passing
25	Passing	Passing	Restricted	Passing	Restricted	Passing	Restricted	Passing	Restricted	Passing	Restricted	Passing
10	Restricted	Passing	Restricted	Passing	Restricted	Passing	Restricted	Passing	Restricted	Passing	Restricted	Passing
5	Restricted	Passing	Restricted	Passing	Restricted	Passing	Restricted	Passing	Restricted	Passing	Restricted	Passing
1	Restricted	Passing	Restricted	Passing	Restricted	Passing	Restricted	Passing	Restricted	Passing	Restricted	Passing

Triplicate experiments were done for each condition. The "passing" of protein molecules through nanofractures when the value of $(F - F_o)$ is greater than zero and "restricted" when the value of $(F - F_o)$ is equal to zero, where F is defined as the mean fluorescence intensity within a specified ROI of the sample in the SW reservoir in the right V-channel at time $t = 180$s and F_o is the baseline fluorescence intensity in the same position at time zero.

bundle of small pores with varied geometry, the area of the largest opening fabricated inside the ABS to be between 2 and 10 nm.

A more quantitative evaluation of the permeability was obtained by monitoring the change in fluorescence intensity over time in the 3D-printed ABS devices. Nanofractures were created with a current threshold of 50 or 25 μA in 1 mM phosphate buffer and the fluorescence intensity of RPE protein quantified from 0 to 180 s at the specified ROI. Figure 4B shows the average and standard deviation of pores created using 25 μA and 50 μA in three devices. Figure 4 shows that the fluorescent intensity of RPE protein increased linearly over time for nanofractures created at both current thresholds with regression coefficients (R^2) of 0.9946 and 0.9875 for 50 μA and 25 μA, respectively. Importantly, the slope of the intensity change is 2.3 times higher at 50 μA than 25 μA, which is very close to the expected twofold increase in the surface area of the nanofracture expected with doubling of the termination current. This shows that using same electrolyte concentration (1 mM phosphate buffer) and similar experimental conditions, nanofractures formed at higher current threshold will produce pores with larger diameter and a higher permeability of protein molecule through the nanofractures compared to smaller current threshold conditions. The relative standard deviation of the slopes determined for three devices using 25 μA and 50 μA was 11.46% and 14.29%, respectively, indicating acceptable interdevice repeatability.

Attempts to fabricate smaller nanofractures by increasing the phosphate buffer concentrations to 100, 250, 500, and 1000 mM, as shown in Table 1, failed to restrict the movement of f-BSA. At all currents and electrolyte concentrations of 100 mM phosphate buffer and above, RPE was restricted from moving through the nanofractures, suggesting little change in the nanofracture size even with a 20-fold change in the conductivity of the electrolyte. These results were unexpected and inconsistent with the work of Shallan et al. with devices made in PDMS where the restricted transport of BSA through the nanofractures fabricated was achieved in similar breakdown system using 1 mM phosphate buffer and a breakdown threshold current of 3 μA [23]. In contrast to the work of Shallan et al. [23], the movement of BSA was found to transport through all nanofractures made at all defined current and electrolyte concentrations in the 3D-printed ABS devices. We believe that the difference in transport properties might be due to the different physical properties of PDMS and ABS. PDMS is elastomeric and flexible, and thus it is possible that the nanofractures relaxed to a smaller size shortly after nanojunction creation, which provided smaller nanofractures than could be achieved in the more rigid ABS. Also, the considerable increase (750 μm) in the gap thickness in ABS device may result in a change of the nanofracture shape. Tahvildari et al. [49] reported slight deviations of the actual nanophore shape from assumed cylindrical geometry with thickness of 20 nm and 10 nm of silicon nitride membranes.

Nevertheless, from the data in Table 1, two trends are apparent. First, as reported previously [23], a lower breakdown current threshold produces smaller nanofractures.

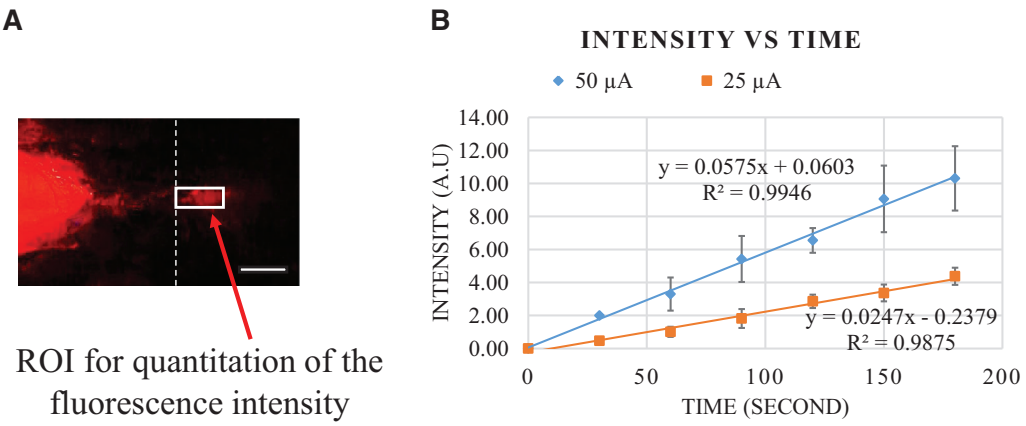

Figure 4. (A) Fluorescence image was opened in image J in RGB scale. Rectangular module was used to draw the region of interest (ROI) (which is 425 µm long and 195 µm wide in this study) and then used the command analyze: measure to obtain the mean fluorescence intensity over time. Scale bar = 400 µm. (B) Graphs shows the mean fluorescence intensity data of the electrophoretic transport of RPE (1 mg/mL) through the nanofractures that formed by using 1 mM phosphate buffer, pH 7 at 50 µA or 25 µA current thresholds at ROI. BGE in the channel during electrophoretic process is 10 mM phosphate buffer, pH 11.5 with 0.5% HPMC. Applied voltage was set at −200 V and +200 V for sample reservoirs (S) and sample wastes reservoirs (SW), respectively. Error bar = mean ± SEM; $n = 3$.

This is evidenced for the transport of RPE with nanofractures made at both 1 mM and 10 mM phosphate buffer. Second, using the same breakdown current threshold, the size of the nanofractures is inversely related to the ionic strength of background electrolyte. This is seen by the movement of RPE being restricted at 100 mM, 50 µA, but passing through the nanofractures at both 10 mM and 1 mM. Also, nanofractures created at 25 µA restricted the movement of RPE at 10 mM but passing through the nanofractures at 1 mM.

These results indicated that both the current threshold and the electrolyte concentration are important parameter to control the nanofracture size. This provides an important insight into the applicability of dielectric breakdown to create nanofractures in point-of-collection devices, where devices and nanofractures have been shown to stop biological macromolecules from interfering with a small molecule assay [23,26]. Initially, it was thought pores could be made before use, allowing devices to be manufactured prefilled with all the reagents, and the nanofractures to be created after placing the sample in the device. Given the influence of the electrolyte concentration on the size of the nanofractures, variation in the sample matrix (e.g., changes in the salinity of urine) may influence the size of the nanofractures formed and hence the transport properties of target analyte within the device, potentially introducing a source of error.

4 Concluding remarks

The creation of nanofractures capable of restricting protein transport movement in ABS 3D-printed microfluidic devices has been demonstrated. The size-selectivity of the nanofracture size was found to depend on both the breakdown current threshold (1-50 µA) and the concentration of the electrolyte (1–1000 mM phosphate pH 7) used for the breakdown process. Low ionic strength electrolytes (1 and 10 mM phosphate buffer) resulted in larger pores, allowing for the passing of RPE when high threshold currents were used (25 µA and 50 µA for 1 mM, 50 µA for 10 mM phosphate buffer, respectively). The nanofractures for current thresholds of 10 µA and below blocked the passage of BSA while permitting the transport of RPE. Additionally, when using electrolyte concentrations of 100–1000 mM all tested current thresholds also restricted the passage of BSA while allowing for the transport of RPE. For nanofractures formed using 1 mM phosphate buffer, increasing the breakdown current from 25 µA and 50 µA was found to increase the flux of RPE through the created pores 2.3-fold. These findings are relevant for the use of controlled dielectric breakdown for the creation of size-selective barriers in devices for point-of-collection testing of pharmaceuticals in body fluids.

The authors would like to thank Dr. Petr Smejkal for his support when operating 3D printing and dielectric breakdown systems. The research was supported by a grant from the Australian Research Council (FT130100101).

The authors have declared no conflict of interest.

5 References

[1] Appenzeller, T., *Science* 1991, *254*, 1300–1302.

[2] Autumn, K., Liang, Y. A., Hsieh, S. T., Zesch, W., Chan, W. P., Kenny, T. W., Fearing, R., Full, R. J., *Nature* 2000, *405*, 681.

[3] Binnig, G., Rohrer, H., Gerber, C., Weibel, E., *Appl. Phys. Lett.* 1982, *40*, 178–180.

[4] Gates, B. D., Xu, Q., Stewart, M., Ryan, D., Willson, C. G., Whitesides, G. M., *Chem. Rev.* 2005, *105*, 1171–1196.

[5] Hunt, H. K., Armani, A. M., *Nanoscale* 2010, *2*, 1544–1559.

[6] Xia, Y., Yang, P., Sun, Y., Wu, Y., Mayers, B., Gates, B., Yin, Y., Kim, F., Yan, H., *Adv. Mater.* 2003, *15*, 353–389.

[7] Feigel, I. M., Vedala, H., Star, A., *J. Mater. Chem.* 2011, *21*, 8940–8954.

[8] Hahm, J.-i., Lieber, C. M., *Nano Lett.* 2004, *4*, 51–54.

[9] Star, A., Gabriel, J.-C. P., Bradley, K., Grüner, G., *Nano Lett.* 2003, *3*, 459–463.

[10] Wang, Y.-C., Stevens, A. L., Han, J., *Anal. Chem.* 2005, *77*, 4293–4299.

[11] Kim, D., Raj, A., Zhu, L., Masel, R. I., Shannon, M. A., *Lab Chip* 2008, *8*, 625–628.

[12] Han, J., Turner, S., Craighead, H. G., *Phys. Rev. Lett.* 1999, *83*, 1688.

[13] Storm, A., Chen, J., Ling, X., Zandbergen, H., Dekker, C., *Nat. Mater.* 2003, *2*, 537.

[14] Kox, R., Chen, C., Maes, G., Lagae, L., Borghs, G., *Nanotechnology* 2009, *20*, 115302.

[15] Yemini, M., Hadad, B., Liebes, Y., Goldner, A., Ashkenasy, N., *Nanotechnology* 2009, *20*, 245302.

[16] Li, J., Stein, D., McMullan, C., Branton, D., Aziz, M. J., Golovchenko, J. A., *Nature* 2001, *412*, 166.

[17] Tang, Z., Zhang, D., Cui, W., Zhang, H., Pang, W., Duan, X., *Nanomater. Nanotechnol.* 2016, *6*, 35.

[18] Sawafta, F., Clancy, B., Carlsen, A. T., Huber, M., Hall, A. R., *Nanoscale* 2014, *6*, 6991–6996.

[19] Mohamed, H., Russo, A. P., Szarowski, D. H., McDonnell, E., Lepak, L. A., Spencer, M. G., Martin, D. L., Caggana, M., Turner, J. N., *J. Chromatogr. A* 2006, *1111*, 214–219.

[20] Li, F., Guijt, R. M., Breadmore, M. C., *Anal. Chem.* 2016, *88*, 8257–8263.

[21] Long, Z., Liu, D., Ye, N., Qin, J., Lin, B., *Electrophoresis* 2006, *27*, 4927–4934.

[22] Tahvildari, R., Beamish, E., Tabard-Cossa, V., Godin, M., *Lab Chip* 2015, *15*, 1407–1411.

[23] Shallan, A. I., Gaudry, A. J., Guijt, R. M., Breadmore, M. C., *Chem. Commun.* 2013, *49*, 2816–2818.

[24] McDonald, J. C., Metallo, S. J., Whitesides, G. M., *Anal. Chem.* 2001, *73*, 5645–5650.

[25] Lee, J. H., Chung, S., Kim, S. J., Han, J., *Anal. Chem.* 2007, *79*, 6868–6873.

[26] Shallan, A. I., Guijt, R. M., Breadmore, M. C., *Angew. Chem. Int. Ed.Engl.* 2015, *54*, 7359–7362.

[27] Al-aqbi, Z. T., Yap, Y. C., Li, F., Breadmore, M. C., *Biosensors* 2019, *9*, 19.

[28] Kwok, H., Briggs, K., Tabard-Cossa, V., *PLoS One* 2014, *9*, e92880.

[29] Briggs, K., Kwok, H., Tabard-Cossa, V., *Small* 2014, *10*, 2077–2086.

[30] Briggs, K., Charron, M., Kwok, H., Le, T., Chahal, S., Bustamante, J., Waugh, M., Tabard-Cossa, V., *Nanotechnology* 2015, *26*, 084004.

[31] Macdonald, N. P., Cabot, J. M., Smejkal, P., Guijt, R. M., Paull, B., Breadmore, M. C., *Anal. Chem.* 2017, *89*, 3858–3866.

[32] Bhargava, K. C., Thompson, B., Malmstadt, N., *Proc. Natl. Acad. Sci. U.S.A.* 2014, *111*, 15013–15018.

[33] Au, A. K., Bhattacharjee, N., Horowitz, L. F., Chang, T. C., Folch, A., *Lab Chip* 2015, *15*, 1934–1941.

[34] Shallan, A. I., Smejkal, P., Corban, M., Guijt, R. M., Breadmore, M. C., *Anal. Chem.* 2014, *86*, 3124–3130.

[35] Cabot, J. M., Fuguet, E., Roses, M., Smejkal, P., Breadmore, M. C., *Anal. Chem.* 2015, *87*, 6165–6172.

[36] Kitson, P. J., Rosnes, M. H., Sans, V., Dragone, V., Cronin, L., *Lab Chip* 2012, *12*, 3267–3271.

[37] Krejcova, L., Nejdl, L., Rodrigo, M. A. M., Zurek, M., Matousek, M., Hynek, D., Zitka, O., Kopel, P., Adam, V., Kizek, R., *Biosens. Bioelectron.* 2014, *54*, 421–427.

[38] Erkal, J. L., Selimovic, A., Gross, B. C., Lockwood, S. Y., Walton, E. L., McNamara, S., Martin, R. S., Spence, D. M., *Lab Chip* 2014, *14*, 2023–2032.

[39] Anderson, K. B., Lockwood, S. Y., Martin, R. S., Spence, D. M., *Anal. Chem.* 2013, *85*, 5622–5626.

[40] Low, Z.-X., Chua, Y. T., Ray, B. M., Mattia, D., Metcalfe, I. S., Patterson, D. A., *J. Membr. Sci.* 2017, *523*, 596–613.

[41] Pinger, C. W., Heller, A. A., Spence, D. M., *Anal. Chem.* 2017, *89*, 7302–7306.

[42] Yuan, S., Strobbe, D., Kruth, J.-P., Van Puyvelde, P., Van der Bruggen, B., *J. Mater. Chem. A.* 2017, *5*, 25401–25409.

[43] Kalsoom, U., Hasan, C. K., Tedone, L., Desire, C., Li, F., Breadmore, M. C., Nesterenko, P. N., Paull, B., *Anal. Chem.* 2018, *90*, 12081–12089.

[44] Li, F., Smejkal, P., Macdonald, N. P., Guijt, R. M., Breadmore, M. C., *Anal. Chem.* 2017, *89*, 4701–4707.

[45] Li, F., Macdonald, N. P., Guijt, R. M., Breadmore, M. C., *Anal. Chem.* 2017, *89*, 12805–12811.

[46] Rosenzweig, D., Carelli, E., Steffen, T., Jarzem, P., Haglund, L., *Int. J. Mol. Sci.* 2015, *16*, 15118–15135.

[47] Monzel, W. J., Hoff, B. W., Maestas, S. S., French, D. M., Hayden, S. C., *IEEE Trans. Dielectr. Electr. Insul.* 2015, *22*, 3543–3549.

[48] Stockert, J. C., Blazquez, A., Galaz, S., Juarranz, A., *Acta Histochem.* 2008, *110*, 333–340.

[49] Tahvildari, R., Beamish, E., Briggs, K., Chagnon-Lessard, S., Sohi, A. N., Han, S., Watts, B., Tabard-Cossa, V., Godin, M., *Small* 2017, *13*, 1602601.

